19th International Conference
ENGINEERING MECHANICS 2013
Svratka, Czech Republic, May 13 – 16, 2013

SPHERICAL NANOINDENTATION APPLIED TO ALUMINIUM FOAM

V. Králík*, J. Němeček**

Abstract: *Nanoindentation is widely used for the assessment of micromechanical behavior of multiple phases within the material microstructure. Evaluation is often restricted to isotropic linearly elastic solids compared to engineering macroscopic tests in which stress–strain curves are analyzed to find variety of constitutive parameters (e.g. viscous, plastic). In this paper, we identify, in addition to the elastic properties, also inelastic properties that can be directly deduced from the load–depth curve of a spherical indentation test through formulations of the effective indentation strain and stress. The accuracy of the determined material properties derived from spherical indentation depends on the accurate knowledge of the indenter shape.. Therefore, calibration and determining the exact geometry of the spherical tip compared with a conical tip is described in details.*

Keywords: ***aluminium foam, porous system, spherical nanoindentation, micromechanical properties, plastic properties.***

1. Introduction

Structural materials (e.g. metals, polymeric or cementitious composites) often exhibit large variation in the microstructure of their solid phases. They are also often characterized by a closed or open pore system. An exceptional example is aluminium foam which typically exhibits macroscopic porosity around 90% of the sample volume. The material is further composed of a network of solid ligaments that are very thin (~60 μm) and microscopically inhomogeneous [Němeček et al. 2012].

However, measurement of mechanical properties of the cell walls is a difficult problem that cannot be solved with conventional methods due to their small dimensions, low local bearing capacity and local yielding and bending of the cell walls. These problems can be overcome using micromechanical methods, namely nanoindentation, in which the load–displacement curve is obtained in the sub-micrometer range independently for distinct microscopic constituents.

Instrumented indentation with spherical indenter is widely used for characterization of local mechanical properties of various materials including metals, ceramics or polymers and offers several advantages comparing to the indentation with sharp indenters. Using spherical indenter, the contact pressure and strains under the indenter are gradually changed as the indentation depth increases while the deformation remains constant in the case of sharp indenters [Johnson, 1985; Fischer-Cripps, 2002; Haušild et al., 2012; Menčík, 2011]. Spherical indentation can be used to investigate hardness (or mean contact pressure) and elastic modulus as a function of penetration depth. It can be further used to compute representative stress-strain curves and to assess plastic properties of the tested material.

In this study an illustrative example of engineering stress-strain curve construction from spherical indentation and plastic parameter identification is shown on aluminum foam cell wall which (due to its small dimensions and hetreogeneous microstructure) requires testing at microscale using nanoindentation.

* Ing. Vlastimil Králík: Faculty of Civil Engineering, Department of Mechanics, Czech Technical University in Prague, Thákurova 2077/7; 166 29, Prague; CZ, e-mail: vlastimil.kralik@fsv.cvut.cz

** Doc. Ing. Jiří Němeček, Ph.D.: Faculty of Civil Engineering, Department of Mechanics, Czech Technical University in Prague, Thákurova 2077/7; 166 29, Prague; CZ, e-mail: jiri.nemecek@fsv.cvut.cz

2. Theory

2.1. Elastic contact

The existing contact mechanics framework [Johnson, 1985; Fischer-Cripps, 2002] for determination of the relationship for indentation stress and strain was considered. Fig. 1 shows the geometry of indentation by a spherical indenter. In contrast to sharp indenters (Vickers, Berkovich), the stresses grow gradually with indenter load. Therefore, spherical indenters enable measurement under relatively low stresses, with all deformations elastic [Johnson, 1985; Menčík, 2011].

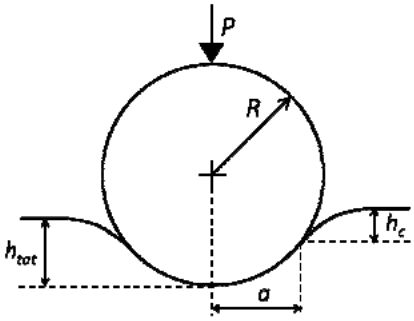

Fig. 1. Indentation by a spherical indenter – geometry

The majority of spherical nanoindentation data analysis is based on the Hertz equation in the elastic region [Johnson, 1985; Fischer-Cripps, 2002; Herbert et al., 2001]:

$$P = \frac{4}{3} E_r R^{1/2} h_{tot}^{3/2} \tag{1}$$

where P is the load, h_{tot} is indenter displacement, R is indenter radius, and E_r is the reduced modulus, related to the elastic modulus E and Poisson´s ratio ν of the sample, through the elastic modulus E_i and Poisson´s ratio ν_i of the indenter (1140 GPa and 0.07) as [Johnson, 1985; Herbert et al., 2001]:

$$1/E_r = (1-\nu^2)/E + (1-\nu_i^2)/E_i \tag{2}$$

The total depth of penetration h_{tot}, contact depth h_c, indenter radius R, contact radius a and area A are related as follows [Fischer-Cripps, 2002; Herbert et al., 2001]:

$$h_c = h_{tot}/2 \tag{3}$$

$$A = \pi a^2 = 2\pi R h_c - h_c^2 \tag{4}$$

Combining Eqs. (1), (3) and (4) yields

$$\frac{P}{\pi a^2} = \frac{4}{3\pi} E_r \left(\frac{a}{R}\right) \tag{5}$$

The left hand side of the equation represents the indentation stress or mean contact pressure [Tabor, 1951]. The expression in parentheses on the right-hand side represents the indentation strain [Tabor, 1951]. Note, these are not same as the stresses and strains measured in uniaxial compression/tension tests but can be related to them [Tabor, 1951].

Elastic modulus can also be obtained using the classic Oliver and Pharr (1992) method. It was showen by the authors that, for all axisymmetric indenters, there is a constant relationship between the elastic contact stiffness S, the contact area A, and the reduced modulus E_r:

$$E_r = \frac{\sqrt{\pi} S}{2\sqrt{A}} \tag{6}$$

The contact depth is defined as [Oliver & Pharr, 1992]:

$$h_c = h_{tot} - \varepsilon \frac{P}{S}, \tag{7}$$

where h_{tot} is the total measured indenter displacement into the sample, and ε is a geometric onstant based on the indenter geometry (ε is 0.75 for a sphere).

In Eq. (6), only the contact stiffness is measured in an experiment. Therefore, for the determination of reduced modulus E_r and also other parameters, such as contact radius a it is necessary to calculate the correct contact area. It is important to note that the contact area should be determined based on the actual geometry of the tip and not just from the nominal radius of the tip (see Chapter 2.3. Indenter calibration).

2.2. Stress – strain diagrams

For elastic–plastic behavior of metals, Tabor (1951) proposed definitions of indentation stress and representative strain. Under a spherical indenter, the contact pressure and strains increase with the depth of indenter penetration, and can be used to construct the conventional uniaxial stress–strain curves. All stress components are proportional to the mean contact pressure P_m, which is very suitable for their characterisation. Indentation (or representative) stress is given by [Tabor, 1951; Haušild et al., 2012; Herbert et al., 2001]:

$$\sigma_{repr} = \frac{P_m}{C} = \frac{P}{C\pi a^2}, \tag{8}$$

where P_m is the mean contact pressure, P is the load and a is the contact radius (see Fig. 1). The parameter C is reffered to as "constraint factor". This factor is actually the degree by which the resistance to plastic flow is higher than the uniaxial flow stress. The increase in this resistance arises mainly form the fact that the plastic zone beneath the indeter is confined by a large volume of material which is elastic. We can distinguish three indentation modes [Taljat et al., 1998; Haušild et al., 2012]:

- Elastic mode - small loads and depth, where the contact is strictly elastic (Herzian)
- Elastic-plastic regime - transition mode in which plasticity begins beneath the surface and C depends on the material hardening
- Fully plastic - in which plasticity extends into the surrounding space. For this reason, the value of C is approximately constant C = 3 for most engineering materials [Tabor, 1951; Haušild et al., 2012; Herbert et al., 2001; Fischer-Cripps, 2002].

Representative (or average indentation) strain is given by:

$$\varepsilon_{repr} = 0.2 \frac{a}{R}, \tag{9}$$

where a is the contact radius, R is the radius of the spherical indenter and prefactor 0.2 was determined empirically by Tabor (1951) on annealed copper and mild steel.

These relations are widely accepted by many authors for estimation of material true stress–strain curves in uniaxial tension or compression [Tabor, 1951; Taljat et al., 1998; Herbert et al., 2001]. It is important to note that Eqs. (8) and (9) are valid only for fully developed plastic contact.

2.3. Indenter calibration

The correct determination of material properties by spherical indenter depends on the exact knowledge of its radius. The indenter shape often deviates from spherical one and the radius is not constant, especially for small tip radii and small depths of penetration. This difference can be quite large see Fig. 2 and 3.

Therefore, the effective radius R_{eff} is used instead of the nominal radius of the tip R [Menčík, 2011]. If the indenter shape is not exactly spherical, various R_{eff} values are obtained for various depths

of penetration. There are different ways to construct the calibration curve R_{eff} (h) or R_{eff} (h_c), respectivelly [Menčík, 2011].

One way is to use the Hertz's solution. By modifying Eq. (1) we obtain:

$$R_{eff}(h) = \frac{9}{16} P^2 E_r^{-2} h^{-3} \tag{10}$$

Using this relationship for each of the measured values of P and h on a sample with known reduced modulus (typically fused quartz) one is able to obtain the calibration curve R_{eff} (h).

Another way is to construct the calibration curve R_{eff} (h) from the "tip area function" $A(h_c)$ by using the Oliver and Pharr (1992) method. To determine the tip area function a series of indents at various contact depths are performed in a sample of known reduced modulus. The contact area for each contact depths is calculated by rearanging Eq. (6). The individual points can be fitted by Eq. (4) to obtain constant value of R_{eff}. This value of R_{eff} represents the average radius for the total indenter penetration h_{tot} with regard to deviations from the ideal spherical shape.

If the shape of the spherical indenter differs significantly from the ideal spherical shape, it is more appropriate to use polynomial fitting function in the form:

$$A(h_c) = C_0 h_c^2 + C_1 h_c + C_2 h_c^{1/2} + C_3 h_c^{1/4} + C_4 h_c^{1/8} + C_5 h_c^{1/16} \tag{11}$$

where h_c is the contact depth and C_0-C_5 are polynomial constants. Once we know the tip area function $A(h_c)$, it is possilble to construct the calibration curve R_{eff} (h_c) using modified Eq. (4).

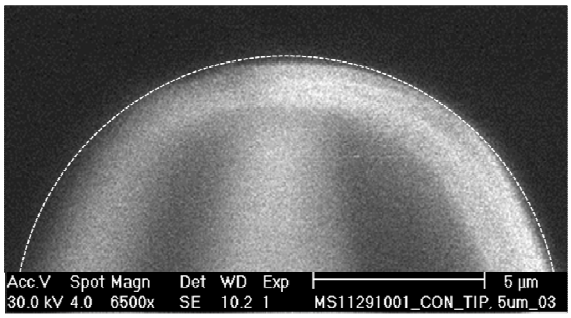

Fig. 2: SEM image of a diamond spheroconical indenter of nominal radius 5 µm (dotted line – ideal radius).

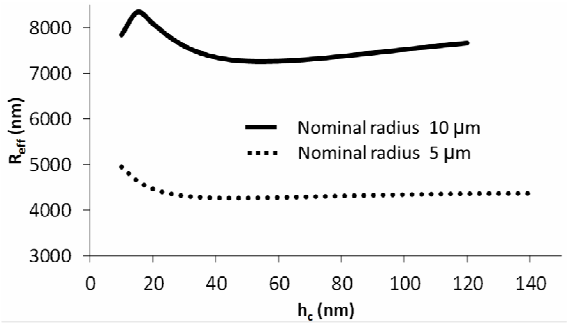

Fig. 3. Effective radius R_{eff} as a function of contact depth h_c. Nominal radius R = 5 µm and R = 10 µm.

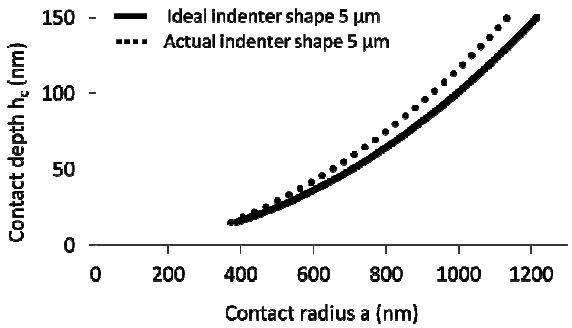

Fig. 4a: Contact depth h_c as a function of actual contact radius a of a spherical indenter with 5 µm nominal radius.

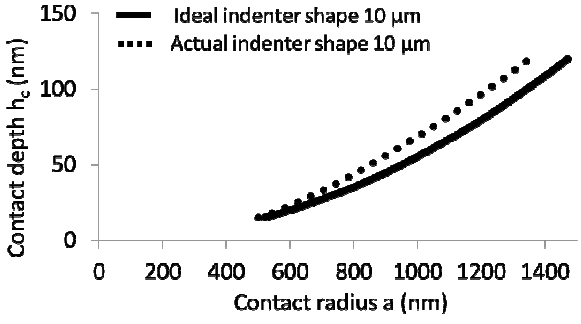

Fig. 4b: Contact depth h_c as a function of actual contact radius a of a spherical indenter with 10 µm nominal radius.

Fig. 3 shows the calibration curve R_{eff} (h_c) for spherical indenters of nominal radius 5 and 10 µm. The curves were obtained from indenter penetration into fused quartz (E_r = 69,6 GPa). The maximum applied load was P = 30 mN for both cases. The corresponding contact depths h_c = 120 nm for indenter of nominal radius 10 µm and h_c = 140 nm for indenter of nominal radius 5 µm were obtained. It can be seen that the effective radius differs significantly from the nominal value 5 µm and 10 µm. It

is also obvious from the graph in Fig. 3 that the function provides unrealiable radius estimates for contact depths less than 30 nm.

Deviations between the actual tip area function $A(h_c)$ and its ideal shape of a spherical tip (using Eq. (4)) are shown in Fig. 4a for 5 μm radius and Fig. 4b for 10 μm radius). As demonstrated by the presented results, an accurate indenter calibration is crucial for correct determination of the material parameters by spherical indenters, especially for small depths of penetration.

3. Experimental methods

Commercial aluminium foam 'Alporas' (Shinko Wire Co., Ltd) was tested in this study. Alporas is an ultra-light weight material with a closed cell structure. An internal structure of the aluminum foam cross section is shown in Fig. 5a on a scale of the whole sample. On a finer scale, microscopically heterogeneous solid ligaments can be found using, e.g. scanning electron microscope (SEM). An example of the cell wall as seen in SEM is shown in Fig. 5b. The majority of the volume (dark zone) is composed of aluminum and aluminium oxide Al_2O_3 (further denoted as Al-rich area). Lighter zones contain significant amount of calcium and titanium (further denoted as Ca/Ti-rich area). Material microstructure and using Berkovich nanoindentation for characterization and modeling of the foam elastic properties is described in detail in [Němeček and Králík, 2012].

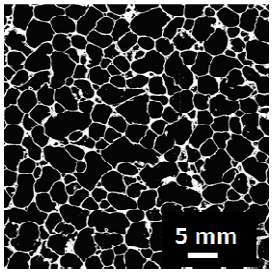

Fig. 5a. Overall view on a typical cross section of aluminium foam Alporas

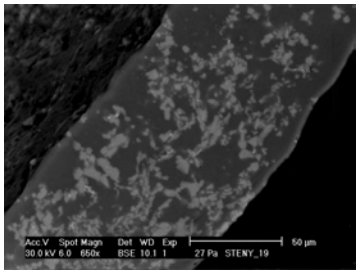

Fig. 5b. SEM image of Alporas cell wall

Nanoindentation measurements were performed on Hysitron Tribolab system® at the CTU in Prague with spherical indenter using instrumented indentation technique [Oliver and Pharr, 1992]. Indenters with small indentation radius (5 μm and 10 μm, resp.) were chosen to achieve fully plastic deformation. Small indenter radii also allow local measurements in the region of very thin cell walls that are typically less than 100 μm wide.

For both indenter tips 4 indents were made at different locations of Al-rich area of the previously polished specimen surface. Partial unloading indentation with increasing load were performed up to maximum load of 3 mN for 10 μm indenter radius and 5 mN for 5 μm indenter radius. Loading time was 5s, followed by 5s holding period at the maximum load and unloading time 5s, per each cycle. Single loading-unloading cycle to the maximum load was also performed for comparison.

4. Results and discussion

Typical load versus indentation depth plot is shown in Fig. 6. Partial unloading indentation and single indentation curves fit closely which justifies evaluation of the representative stress and representative strain from individual cycles in the partial unloading indentation diagram. Therefore, indentation load and depth data from individual cycles were used for the construction of the true stress-strain diagram as shown in Fig. 7 (using Eqs. (8) and (9)). Since strains derived indentation measurements lie in the plastic region an average elastic modulus (Tab.1) was used for the construction of elastic part of the stress-strain curve in Fig. 7.

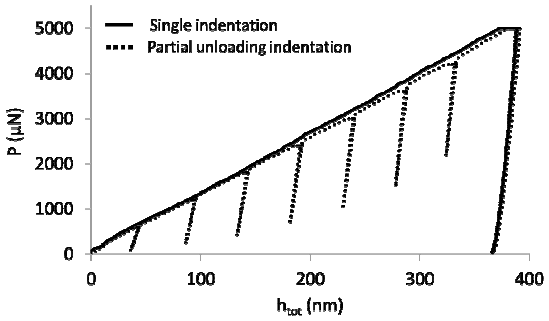

Fig. 6. Typical single and partial unloading indentation load vs. depth curve (Alporas cell wall, Al-rich phase, 5μm indenter radius)

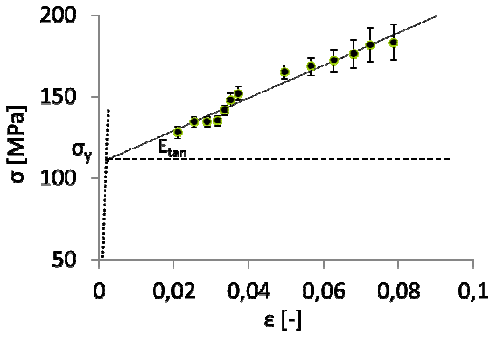

Fig. 7. Stress–strain relations obtained by nanoindentation with different indenter radii (Alporas cell wall, Al-rich phase)

It can be seen in Fig. 7 there is a smooth transition between measured data for both tips radii evaluated for strain larger than ~0.02. It seems that for small representative strains it is suitable to use a larger indenter radius (keeping the low indentation depths but increasing the indentation contact area), but we have to remain in the fully plastic regime [Herbert et al., 2001]. Based on the recent finite element investigations of Mesarovic & Fleck (1999), this regime occurs when $a/R \approx 0.16$.

For small measured contact depths (up to about 60 nm), there are considerable differences in the evaluated data of the true stress-strain. These differences may be caused by imperfect shape of the spherical indenter for small contact depths and/or surface roughness of the sample. Therefore measured data for the contact depth up to 60 nm were not evaluated.

Once the uniaxial stress-strain diagram (Fig. 7) is constructed constitutive parameters related to plastic material can be deduced. As a first approximation, an elasto-plastic material model with isotropic linear hardening can be assumed. Then, the plastic parameters are described by two constants, the yield point (σ_y) and tangent modulus (E_{tan}) as depicted in Fig. 7. Since the data points are obtained for strains exceeding the elastic limit it is necessary to assess the elastic modulus independently. The elastic modulus was evaluated for individual indents at each unloading cycle (Fig. 6) using standard Oliver and Pharr methodology. Resulting elastic modulus $E_{Al} = 57.1 \pm 4.4$ GPa was obtained by averaging results from all cycles of selected curves (n=7) lying in the Al-rich phase.

The tangent modulus was obtained by the least square fitting of the measured points (Fig. 7) using linear approximation. The yield point was found as an intersection of elastic and plastic branches in the diagram (Fig. 7). The evaluated elastic and plastic parameters of Al-rich phase of the material are listed in Tab. 1. The elastic modulus is in good agreement with the data received from Berkovich indentation and statistical deconvolution [Němeček and Králík, 2012]. The yield point exhibits also small scatter of values.The relatively larger variance in values of tangent modulus (E_{tan}) is probably due to the heterogeneity of the material which is more pronounced in larger indentation depths. As the indentation depth and volume increases, the mutual influence between the material phases (Al-rich and Ca/Ti-rich) that can found in the vicinity of the indent or below the surface is also increasing.

Tab. 1: Resulting material constants for Alporas cell wall, Al-rich phase.

Elastic modulus	E [GPa]	57.1 ± 4.4
Yield point	σ_y [MPa]	111.1 ± 0.6
Tangent modulus	E_{tan} [MPa]	1001.6 ± 112.7

Unfortunately, due to the manufacturing process of the porous aluminium foam (see Mioshy et al., 1998), there are no available data from measurements of stress-strain diagram evaluated directly from a uniaxial tensile test on the raw material. On the other hand, values of the measured elastic modulus (E) and yield strength (σ_y) are in good agreement with data reported for Alporas foam by Zlámal et al. (2012) who derived the material constants based on FE model and optimal fitting of nanoindentation

experiment. Further validation of the results and comparison with measured data from tensile tests on a similar aluminum material is proposed as a future goal.

5. Conclusions

It was shown in the paper that spherical nanoindentation provides a reasonable framework for the assessment of elastic as well as inelastic parameters of material constituents at microscale. The methodology was illustrated on the case of aluminium foam.

The partial unloading nanoindentation technique with two different indenter radii was used for the prediction of the local mechanical behavior of Al-rich phase on the aluminium foam cell wall in the fully plastic regime. Stress–strain relations were constructed from nanoindentation experiment using Tabor's formulae. Elastic properties evaluated for individual indents in the prevailing Al-rich phase at each indentation cycle was evaluated using standard Oliver and Pharr method which fully relies on the accurate knowledge of the indenter shape. Therefore, careful indenter calibration was performed together with estimation of the effective tip radius. The calibration procedures were discussed in details in the paper. Resulting elastic modulus of evaluated indents reached $E_{Al} = 57.1 \pm 4.4$ GPa. Plastic parameters of the Al-rich phase in the material were assessed from stress-strain diagrams assuming elasto-plastic material model with linear isotropic hardening. The Al-rich phase was characterized with the yield point $\sigma_y \approx 111.1 \pm 0.6$ MPa and tangent modulus $E_{tan} \approx 1001.6 \pm 112.7$ MPa. Due to the lack of direct tension/compression data of the raw material in the literature, the results obtained from nanoindentation could not be compared to their uniaxial counterparts. However, the values are in good agreement with the range of values based on FEM model reported for Alporas® by Zlámal et al. (2012).

Further research and identification of the material parameters using FEM analyses of spherical indentations is planned in the near future.

Acknowledgement

Support of the Czech Science Foundation (GAČR P105/12/0824) and the Grant Agency of the Czech Technical University in Prague (SGS12/116/OHK1/2T/11) is gratefully acknowledged.

References

Fischer-Cripps A.C. (2002) *Nanoindentation.* Springer Verlag, ISBN 0-387-95394-9.

Haušild P., Materna A., Nohava J. (2012) On the identification of stress–strain relation by instrumented indentation with spherical indenter, Materials and Design, 37, pp. 373-378.

Herbert E.G., Pharr G.M., Oliver W.C., Lucas B.N., Hay J.L. (2001) On the measurement of stress–strain curves by spherical indentation, Thin Solid Films, 398–399, pp. 331–335.

Johnson K.L. (1985) *Contact Mechanics.*Cambridge University Press, Cambridge.

Menčík J. (2011) Opportunities and problems in nanoindentation with spherical indenters, Chemické Listy, 105, pp. 680-683

Mesarovic S.D., Fleck N.A. (1999) Spherical indentation of elastic–plastic solids, Proc. Royal Soc. Lond., 455, pp. 2707–2728.

Miyoshi T., Itoh M., Akiyama S. & Kitahara A. (1998) Aluminium foam, "ALPORAS": The production process, properties and application, Mat. Res. Soc. Symp. Proc., 521, pp.133-137.

Němeček J., Králík V. (2012) A two-scale micromechanical model for closed-cell aluminium foams, in: B.H.V. Topping, editor, Proceedings of the Eleventh International Conference on Computational Structures Technology, (Stirlingshire: Civil-Comp Press), pp. 391–397.

Oliver W. & Pharr G. (1992) An improved technique for determining hardness and elastic modulus using load and displacement sensing indentation experiments, Journal of Material Research, 7, 6, pp.1564-1583.

Tabor D. (1951) *Hardness of Metals*. Clarendon Press, Oxford.

Taljat B., Zacharia T., Kosel F. (1998) New analytical procedure to determine stress–strain curve from spherical indentation data, Int J Solid Struct, 35, pp. 4411–26.

Zlámal P., Jiroušek O., Králík V. (2012) Identification of elasto-visco-plastic constitutive material model with damage for porous material based on the indirect finite element simulation of the nanoindentation test, in: *Proceedings of the 13th Bilateral Czech/German Symposium* (CTU in Prague, Faculty of Transportation Sciences), pp. 107-110.